

# On the Relationship Between Hydrogen-Bonding Motifs and the $1b_1$ Splitting in the X-ray Emission Spectrum of Liquid Water

*Vinicius Wilian D. Cruzeiro*<sup>1,2,\*</sup>, *Andrew P. Wildman*<sup>3</sup>, *Xiaosong Li*<sup>3</sup>, *Francesco Paesani*<sup>1,2,4,\*</sup>

<sup>1</sup> San Diego Supercomputer Center, University of California San Diego, La Jolla, CA 92093,  
United States

<sup>2</sup> Department of Chemistry and Biochemistry, University of California San Diego, La Jolla, CA  
92093, United States

<sup>3</sup> Department of Chemistry, University of Washington, Seattle, WA, 98195, United States

<sup>4</sup> Materials Science and Engineering, University of California San Diego, La Jolla, CA 92093,  
United States

\* E-mails: [vcruzeiro@ucsd.edu](mailto:vcruzeiro@ucsd.edu), [fpaesani@ucsd.edu](mailto:fpaesani@ucsd.edu)

## ABSTRACT

The split of the  $1b_1$  peak observed in the X-ray emission (XE) spectrum of liquid water has been the focus of intense research over the last two decades. Although several hypotheses have been proposed to explain the origin of the  $1b_1$  splitting, a general consensus has not yet been reached. In this study, we introduce a novel theoretical/computational approach which, combining path-integral molecular dynamics (PIMD) simulations carried out with the MB-pol potential energy function and time-dependent density functional theory (TD-DFT) calculations, correctly predicts the split of the  $1b_1$  peak in liquid water and not in crystalline ice. A systematic analysis in terms of the underlying local structure of liquid water at ambient conditions indicates that several different hydrogen-bonding motifs contribute to the overall XE lineshape in the energy range corresponding to emissions from the  $1b_1$  orbitals, which suggests that it is not possible to unambiguously attribute the split of the  $1b_1$  peak to only two specific structural arrangements of the underlying hydrogen-bonding network.

## INTRODUCTION

Liquid water displays a unique behavior that manifests in an anomalous temperature dependence of several thermodynamic properties (e.g., density, heat capacity, and compressibility) as it is cooled to lower temperatures.<sup>1,2</sup> At the electronic structure level, besides the core  $1s$  orbital of the oxygen atom ( $1a_1$ ) and the bonding  $2a_1$  orbital, an isolated water molecule is characterized by three occupied valence orbitals corresponding to the bonding  $1b_2$  and  $3a_1$  orbitals and the non-bonding  $1b_1$  lone-pair orbital. The two lowest unoccupied orbitals correspond to the anti-bonding  $4a_1$  and  $2b_2$  orbitals (Fig. 1a). Although in the condensed phases (i.e., liquid water and ice) the valence orbitals are still primarily localized on each molecule, they are also sensitive to variations in the structure of the surrounding hydrogen-bonding (H-bonding) network. By exploiting the correlation between orbital energies and H-bonding motifs, X-ray absorption (XA) and emission (XE) spectroscopies have emerged as powerful techniques to probe the local structure of liquid water.<sup>3</sup> XA spectroscopy measures transitions from the  $1a_1$  orbital to one of the unoccupied orbitals, which are induced by absorption of X-rays, while XE spectroscopy measures the subsequent transition from an occupied valence orbital to the emptied  $1a_1$  orbital, which is accompanied by the emission of an X-ray photon.

Emission transitions from the  $1b_1$  orbitals give rise to two sharp peaks ( $1b'_1$  and  $1b''_1$ ) in the XE spectrum of liquid water, with the relative intensities of the two peaks varying appreciably as the temperature is decreased from 338.15 K to 280.15 K.<sup>4</sup> In contrast, the XE spectrum of ice displays a single peak, with maximum intensity in correspondence to the  $1b'_1$  peak of liquid water, and only a shoulder at relatively higher emission energies in correspondence to the  $1b''_1$  peak of liquid water. The presence of distinct  $1b'_1$  and  $1b''_1$  peaks in the XE spectrum of liquid water has attracted particular interest, both experimentally and theoretically. As a result, several

hypotheses have been proposed to explain the split of the  $1b_1$  peak, connecting its origin to local H-bonding environments,<sup>1,5-7</sup> two different structural motifs,<sup>1,4,8-11</sup> ultrafast dissociation,<sup>12,13</sup> and coupling between emissions from the  $1b_1$  and  $3a_1$  orbitals.<sup>14</sup> Despite the development of several theoretical and computational approaches for modeling the XE spectrum of liquid water,<sup>5-7,9,14,15</sup> a precise reproduction of the  $1b_1$  splitting has so far remained elusive.

Simulations of the XE spectrum of liquid water are particularly challenging since they are sensitive to the choice of the molecular model used to describe the liquid structure as well as to the level of theory used to calculate the relevant electronic transitions. In an attempt to address both challenges, in this study we introduce a novel theoretical/computational approach that combines path-integral molecular dynamics (PIMD)<sup>16-19</sup> simulations, carried out with the MB-pol potential energy function (PEF),<sup>20-22</sup> and time-dependent density functional theory (TD-DFT)<sup>23-25</sup> within the quantum mechanics/molecular mechanics (QM/MM) formalism. Since all specific details are provided in the Methods section, we only summarize here the main features of our approach. Briefly, PIMD is based on Feynman's path-integral formulation of statistical mechanics<sup>26</sup> and allows for a quantitative account of nuclear quantum effects in liquid water.<sup>27,28</sup> MB-pol has been shown to correctly predict the structural, thermodynamic, dynamical, and spectroscopic properties of water from the gas to the condensed phase,<sup>29,30</sup> quantitatively reproducing the vibration-rotation tunneling spectrum of the water dimer,<sup>20</sup> the energetics, quantum equilibria, and infrared spectra of small water clusters,<sup>22,31,32</sup> and the temperature-dependence of various properties of liquid water and ice.<sup>21,30,33-41</sup> More recently, molecular configurations extracted from PIMD simulations carried out with MB-pol have been used in many-body perturbation theory electronic structure calculations to model the electron affinity<sup>42</sup> and the XA spectrum<sup>43</sup> of liquid water. Finally, TD-DFT enables calculations of electronic

transitions between well-defined initial and final states.<sup>23–25</sup> This makes TD-DFT well suited to investigate the  $1b_1$  splitting in the XE spectrum of liquid water which is associated with transitions from  $1b_1$  to  $1a_1$  orbitals (Fig. 1a).

## RESULTS

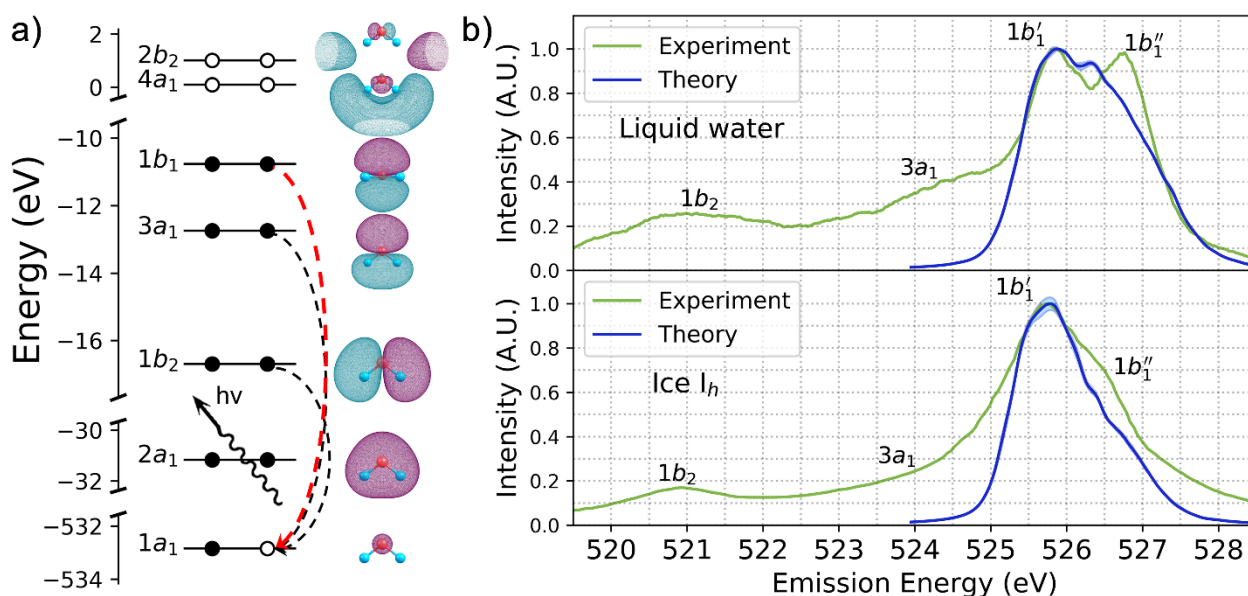


**Figure 1.** a) Schematic representation of the transitions measured in the XE spectrum of liquid water and ice (dashed arrows). The dashed red arrow represents the process modeled by the QM/MM TD-DFT calculations presented in this study. b) Green: Experimental XES of liquid water at 311 K (top panel)<sup>4</sup> and ice  $I_h$  at 263 K (bottom panel).<sup>44</sup> Blue: Theoretical  $1b_1$ -to- $1a_1$  lineshapes calculated for liquid water at 298.15 K (top panel) and ice  $I_h$  at 200 K (bottom panel).

The experimental XE spectra of liquid water at 311 K<sup>4</sup> and ice  $I_h$  at 263 K<sup>44</sup> are compared in Fig. 1b with the theoretical  $1b_1$ -to- $1a_1$  lineshapes obtained from the QM/MM TD-DFT calculations. Nearly quantitative agreement is observed between theory and experiment for ice  $I_h$ , although the theoretical lineshape lacks intensity between 526 eV and 527 eV, in correspondence of the  $1b_1''$

shoulder. In the case of liquid water, the theoretical lineshape correctly captures the overall linewidth, although the experimentally observed  $1b_1$  splitting is significantly underestimated. Only a minor peak is observed at  $\sim 526.3$  eV, which is possibly related to the  $1b_1''$  peak. Importantly, as in the case of ice  $I_h$ , the theoretical lineshape for liquid water also lacks intensity at relatively higher emission energies between 526.5 eV and 527.3 eV, which corresponds to the energy range associated with the  $1b_1''$  peak observed in the experimental XE spectrum. Considering that ice  $I_h$  consists of only one (completely tetrahedral) H-bonding motif, the lack of intensity in correspondence of the  $1b_1''$  feature in the theoretical lineshapes of both crystalline ice and liquid water suggests that the appearance of a distinct  $1b_1''$  peak in the experimental XE spectrum of liquid water may not exclusively be due to the interplay between different H-bonding motifs. For comparison, Fig. S1 of the Supporting Information shows the Delta SCF XE spectrum obtained with the same level of theory used in the QM/MM TD-DFT calculations. As shown in previous studies,<sup>7</sup> while Delta SCF calculations allow for modeling transitions from all three valence orbitals, they predict a featureless  $1b_1$  peak, which is significantly narrower than in the experimental XE spectrum. This likely arises from the well-known Delta SCF limitation in describing the excited state as not orthogonal to the variational ground state of the system.<sup>45</sup>

## DISCUSSION

Based on the agreement between the experimental and theoretical lineshapes found for ice  $I_h$  in Fig. 1b, we investigate possible reasons for the lower intensity of the  $1b_1''$  peak predicted by the QM/MM TD-DFT calculations of liquid water to provide insights into the correlation between the  $1b_1$ -to- $1a_1$  lineshape and the underlying H-bonding motifs. For these analyses, we consider all H-bonding topologies<sup>46</sup> involving the central QM water molecule, which are determined

using the definition of H-bonds described in Ref. 47. In this regard, it should be noted that, since our QM/MM TD-DFT calculations are performed on molecular configurations extracted from PIMD simulations with MB-pol, which is a non-dissociable water model, we are not in the position to determine possible contributions due to the presence of both undissociated and dissociated water molecules, which was suggested in Refs. 12 and 13 as a possible origin for the  $1b_1$  splitting. Furthermore, since our QM/MM TD-DFT calculations only probe  $1b_1$ -to- $1a_1$  transitions, they do not report on possible contributions arising from the coupling between  $1b_1$  and  $3a_1$  emissions, which was proposed in Ref. 14 to explain the split of the  $1b_1$  peak.

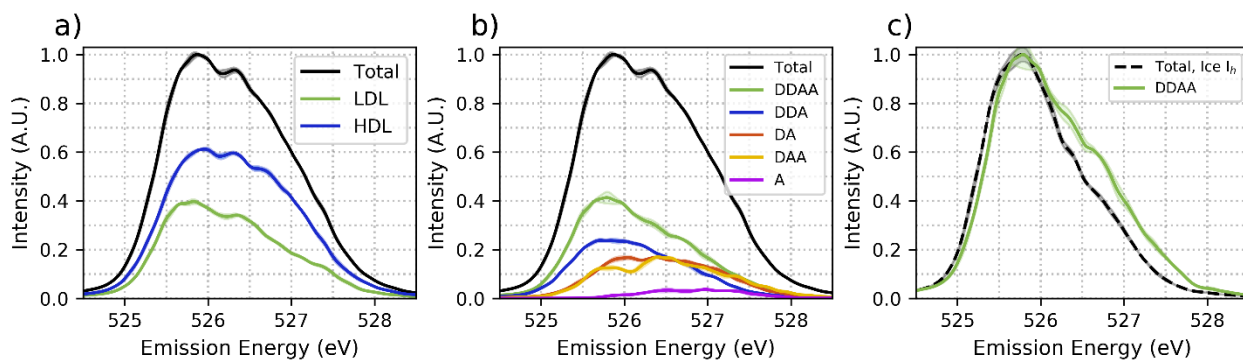


**Figure 2.** Analyses of the theoretical  $1b_1$ -to- $1a_1$  lineshape of liquid water in terms of different H-bonding motifs. a) Contributions from high-density liquid (HDL) and low-density liquid (LDL) structures. b) Contributions from individual H-bonding topologies (for clarity, only contributions from H-bonding topologies with the five largest fractions, corresponding to more than 90% of the total number of structures sampled in the MB-pol PIMD simulations, are shown). c) Comparison between the theoretical  $1b_1$ -to- $1a_1$  lineshape associated with tetrahedral (DDAA) structures in liquid water and the total  $1b_1$ -to- $1a_1$  lineshape calculated for ice  $I_h$ . D = donor and A = acceptor in both panels b) and c).

Several interpretations of the  $1b_1$  splitting in the experimental XE spectrum of liquid water have been put forward, which connect the presence of the  $1b_1'$  and  $1b_1''$  peaks to specific structural

arrangements of the underlying H-bonding network. In particular, it was proposed that the split of the  $1b_1$  peak may result from the presence of two distinct structural motifs,<sup>1,7,9-11</sup> commonly referred to as low-density liquid (LDL) and high-density liquid (HDL), which are thought to be responsible for the  $1b'_1$  and  $1b''_1$  peaks, respectively. To test this hypothesis, we follow Ref. 11 and adopt the local structure index (LSI) to classify the water configurations used in our QM/MM TD-DFT calculations as either LDL ( $LSI > 0.03 \text{ \AA}^2$ ) or HDL ( $LSI < 0.03 \text{ \AA}^2$ ). Specific details about this classification are given in the Supporting Information. The analysis of the theoretical lineshape shown in Fig. 2a indicates that both HDL and LDL configurations extracted from the MB-pol PIMD simulations contribute to transitions that span the entire energy range associated with the  $1b_1$ -to- $1a_1$  lineshape. Although this analysis suggests that it is not possible to unambiguously assign the  $1b'_1$  and  $1b''_1$  peaks to LDL and HDL motifs,<sup>1,7,9-11</sup> Fig. 2a shows that LDL structures are, on average, associated with lower transition energies, which is in line, at least qualitatively, with the hypothesis that identifies these configurations as responsible for the  $1b'_1$  peak.

A different but closely related hypothesis suggests that the  $1b'_1$  peak is associated with tetrahedral H-bonding arrangements, while the  $1b''_1$  peak arises from all other H-bonding motifs.<sup>1,4,8</sup> To test this hypothesis, the theoretical  $1b_1$ -to- $1a_1$  lineshape is dissected in Fig. 2b into contributions from individual H-bonding topologies associated with the underlying equilibrium distributions of molecular configurations. For clarity, Fig. 2b only shows contributions from double donor–double acceptor (DDAA), double donor–single acceptor (DDA), single acceptor–single donor (DA), single donor–double acceptor (DAA), and single acceptor (A) topologies, which make up 92.4% of all configurations sampled in the MB-pol PIMD simulations of liquid water. Contributions to the theoretical  $1b_1$ -to- $1a_1$  lineshape from all

remaining H-bonding topologies are shown in Fig. S3, while the complete list of H-bonding topologies, along with the corresponding fractions, is reported in Table S1 of the Supporting Information. Fig. 2b shows that DDAA configurations, which correspond to tetrahedral H-bonding arrangements, are characterized by  $1a_1$ -to- $1b_1$  transition energies that span the entire lineshape. It should be noted, however, that the distribution of DDAA transition energies exhibits a maximum in correspondence of the  $1b_1'$  peak, which is in qualitative agreement with the proposed hypothesis.<sup>1,4,8</sup> Importantly, as shown in Fig. 2b, the theoretical lineshape due to only DDAA structures found in liquid water overlaps, nearly exactly, with the total  $1b_1$ -to- $1a_1$  lineshape calculated for ice  $I_h$ . While, on one hand, this analysis indicates that the disappearance of a distinct  $1b_1''$  peak in the experimental XE spectrum of crystalline ice is indeed related to the absence of H-bonding topologies different from the DDAA motif, in agreement with previous interpretations of the experimental XE spectrum of ice,<sup>1,4,8</sup> on the other hand, the lack of intensity between 526.5 eV and 527.3 eV in the theoretical  $1b_1$ -to- $1a_1$  lineshape of ice  $I_h$  suggests that the variations in relative intensity of the  $1b_1'$  and  $1b_1''$  peaks, observed in the experimental XE spectra of crystalline ice and liquid water as a function of temperature, may not only be attributed to changes in the underlying H-bonding network. In this context, it should be noted that the differences between the experimental and theoretical lineshapes in the 526.5 eV to 527.3 eV energy range may also be related to inherent inaccuracies in the TD-DFT representation of the  $1b_1$ -to- $1a_1$  transitions.

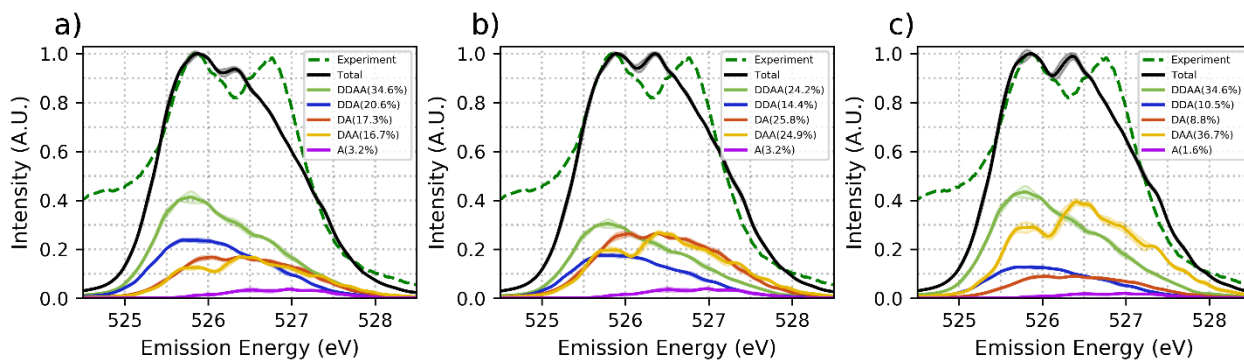


**Figure 3.** Comparison between theoretical  $1b_1$ -to- $1a_1$  lineshapes of liquid water calculated for: a) the original distribution of H-bonding topologies identified in the MB-pol PIMD simulations (as in Fig. 2b), and two hypothetical distributions with larger fractions of single-donor configurations. Specifically, in b) and c) the original fractions of individual H-bonding topologies are artificially modified in order to increase the total fraction of single-donor configurations, 49.1% in b) and 33.8% in c), while reducing the total fraction of double-donor configurations, 30.1% in b) and 18.3% in c).

To further analyze the relationship between the XE spectrum and the structure of the underlying H-bonding network in liquid water, in the following we investigate the effects of different H-bonding topologies on the  $1b_1$ -to- $1a_1$  transitions, in an attempt to identify specific distributions of H-bonding configurations that may lead to a more defined split of the  $1b_1$  peak in the theoretical lineshape. For this purpose, the original distribution of H-bonding topologies extracted from the MB-pol PIMD simulations of liquid water at 298.15 K are artificially modified to generate two hypothetical H-bonding distributions with reduced fractions of double-donor configurations and increased fractions of single-donor configurations. Fig. 3 shows a comparison between the theoretical  $1b_1$ -to- $1a_1$  lineshapes calculated with the original fractions of H-bonding topologies (Fig. 3a) and two significantly different distributions of H-bonding topologies, where the total fraction of single-donor configurations is increased to 49.1% (Fig. 3b)

and 33.8% (Fig. 3c) and the total fraction of double-donor configurations is reduced to 30.1% (Fig. 3b) and 18.3% in (Fig. 3c). Although the theoretical  $1b_1$ -to- $1a_1$  lineshapes associated with the two hypothetical H-bonding distributions exhibit a slightly more pronounced peak at 526.3 eV relative to the original lineshape, the position of this peak is still  $\sim 0.4$  eV to the left of the  $1b_1''$  peak observed in the experimental XES spectrum. This analysis indicates that, given the broad energy distributions associated with the different H-bonding topologies, it is not possible, within our model of the  $1b_1$ -to- $1a_1$  lineshape, to generate any combination of H-bonding topologies that can lead to well-defined  $1b_1'$  and  $1b_1''$  peaks as observed in the experimental XE spectrum.

The analyses of the theoretical  $1b_1$ -to- $1a_1$  lineshape in terms of different H-bonding topologies shown in Figs. 2 and 3 indicate that molecular configurations in which the central water molecule donates two hydrogen bonds (i.e., DDAA and DDA topologies) are primarily associated with lower emission energies. In contrast, molecular configurations in which the central water molecule donates only one hydrogen bond (i.e., DA and DAA topologies) primarily contribute to the high energy portion of the theoretical lineshape. In particular, it can be noted that removing a donating hydrogen bond from a DDAA configuration shifts the contribution of the resulting DAA configuration to higher emission energies. On the other hand, removing an accepting hydrogen bond from a DDAA configuration results in a DDA configuration whose contribution shifts to lower emission energies. Importantly, breaking a donating hydrogen bond appears to have a significantly larger effect on the theoretical  $1b_1$ -to- $1a_1$  lineshape than breaking an accepting hydrogen bond. This analysis suggests that the  $1b_1'$  peak can be primarily associated with double-donor configurations while the  $1b_1''$  peak mainly arises from single-donor configurations. This observation is further illustrated in Fig. 4, where the theoretical  $1b_1$ -to- $1a_1$

lineshape is dissected into contributions from double-donor (i.e., DDAA + DDA) and single-donor (i.e., DA + DAA) configurations. Although the contributions from double-donor and single-donor configurations extend over a wide range of emission energies, the corresponding energy distributions display maxima at emission energies that are approximately centered in correspondence of the  $1b_1'$  and  $1b_1''$  peaks, respectively.

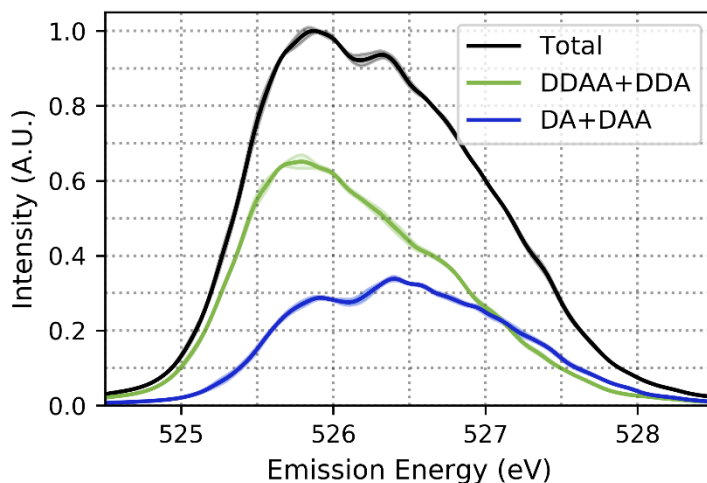


**Figure 4.** Theoretical  $1b_1$ -to- $1a_1$  lineshape of liquid water dissected into contributions from double-donor (green) and single-donor (blue) H-bonding motifs. D = donor and A = acceptor.

In conclusion, we have introduced a novel theoretical/computational approach to model the  $1b_1$ -to- $1a_1$  portion of the XE spectrum of liquid water and ice, which uses molecular configurations extracted from PIMD simulations with the MB-pol PEF in subsequent TD-DFT calculations. Although the theoretical  $1b_1$ -to- $1a_1$  lineshape is found to be in good agreement with the experimental spectrum of crystalline ice, it lacks intensity between 526.5 eV and 527.3 eV, which corresponds to the range of emission energies assigned to the  $1b_1''$  feature. A similar trend is found in the theoretical  $1b_1$ -to- $1a_1$  lineshape of liquid water which, consequently, is unable to quantitatively reproduce the  $1b_1$  splitting observed in the corresponding experimental XE

spectrum. Although our model does not allow for determining possible contributions to the  $1b_1$ -to- $1a_1$  lineshape due to the simultaneous presence of undissociated and dissociated water molecules, and/or to couplings between  $1b_1$  and  $3a_1$  emissions, it provides an effective theoretical/computational framework to investigate contributions associated with different H-bonding motifs. In particular, while it is found that double-donor and single-donor configurations have higher probabilities to emit at lower and higher energies, respectively, our analyses indicate that all H-bonding topologies are associated with broad emission energy distributions that span the entire energy range of the  $1b_1$ -to- $1a_1$  lineshape. This effectively precludes a one-to-one assignment of the  $1b_1'$  and  $1b_1''$  peaks observed in the experimental XE spectrum to only two specific H-bonding motifs. In an attempt to recover the experimental  $1b_1$  splitting, the  $1b_1$ -to- $1a_1$  lineshape has also been calculated for hypothetical H-bonding distributions, with increased fractions of single-donor configurations. Although the theoretical lineshapes corresponding to these hypothetical H-bonding distributions display a slightly more pronounced peak at higher emission energies, they still largely underestimate the intensity in the energy range associated with the experimental  $1b_1''$  peak.

Within the approximations of our theoretical model, the analyses presented in this study suggest that, while different H-bonding motifs are found to contribute differently to the overall  $1b_1$ -to- $1a_1$  lineshape, it is not possible to attribute the appearance of well-defined  $1b_1'$  and  $1b_1''$  peaks in the experimental XE spectrum of liquid water to any specific structural arrangements of the underlying H-bonding network. In the future, it would be important to repeat the present QM/MM calculations of the  $1b_1$ -to- $1a_1$  transitions using more accurate electronic structure methods (e.g., equation-of-motion coupled cluster theory) whose computational cost is currently prohibitively expensive. By providing a quantitative assessment of the sensitivity of the overall

$1b_1$ -to- $1a_1$  lineshape to the representation of the relevant electronic transitions, these calculations will allow for a more direct comparison between the experimental and theoretical XE spectra of liquid water.

## METHODS

To model the  $1b_1$ -to- $1a_1$  transitions, molecular configurations of liquid water at 298.15 K and ice I<sub>h</sub> at 200 K are extracted from PIMD simulations carried out with MB-pol.<sup>21</sup> These configurations are then used in quantum mechanics/molecular mechanics (QM/MM) TD-DFT calculations in which a given number of water molecules ( $N_{H_2O}$ ), defining a central cluster, are treated at the QM level of theory using the BHandH exchange-correlation functional<sup>48</sup> in combination with the aug-cc-pCVTZ basis set<sup>49</sup> and aug-cc-pVTZ basis set<sup>50</sup> for, respectively, the oxygen and the hydrogens in the central water molecule, and the aug-cc-pVDZ basis set<sup>50</sup> for the remaining  $N_{H_2O} - 1$  molecules. All other molecules within 20 Å from the central molecule are represented as point charges located on the oxygen and hydrogen atoms in order to mimic the condensed phase environments corresponding to liquid water and ice. The values of the point charges are taken from the q-SPC/Fw water model.<sup>51</sup> It should be noted that the BHandH functional has been previously shown to reproduce near-edge XA spectroscopy with low error,<sup>52-54</sup> and it has recently been suggested that using basis sets of triple-zeta quality with split-core at the core-excitation site improves the description of core excitations.<sup>55</sup> All QM/MM TD-DFT calculations were performed with Gaussian 16.<sup>56</sup> Since PIMD simulations with MB-pol predict a first solvation shell of 4.8 molecules for liquid water at 298.15 K,<sup>21</sup> a total of 6 water molecules (i.e.,  $N_{H_2O} = 6$ ), corresponding to a central molecule and its 5 closest neighbors, are included in the QM region of the QM/MM TD-DFT calculations for liquid water. On the other hand, since

each water molecule is tetrahedrally coordinated in crystalline ice, the QM/MM TD-DFT calculations for ice I<sub>h</sub> are carried with 5 molecules in the QM region. For further comparisons, a QM region consisting of 6 water molecules is also considered for ice I<sub>h</sub> and the corresponding XE spectrum is reported in Fig. S2 at the Supporting Information.

Since conventional TD-DFT calculations are unable to handle the presence of a hole in a core orbital, we effectively simulate the inverse XE process (Fig. 1a) by placing the hole in the valence  $1b_1$  orbital and calculating the energy difference between the  $1a_1$  and  $1b_1$  orbitals. The actual XE spectrum in the  $1b_1$  region is then obtained by considering only transitions for QM/MM configurations where both the  $1a_1$  and  $1b_1$  orbitals are localized on the central molecule of the QM cluster. It should be noted that the full XE spectrum can, in principle, be calculated from Delta SCF calculations.<sup>57,58</sup> However, due to non-orthogonality between the variational ground state and an excited state obtained through Delta SCF, Delta SCF calculations suffer from inherent limitations, often leading to incorrect localization of ionized states which negatively impact their accuracy.<sup>45</sup> Specific details about the present QM/MM TD-DFT calculations are reported in the Supporting Information.

## **DATA AVAILABILITY**

Any data generated and analyzed for this study that are not included in this article and its Supplementary Information are available from the authors upon request.

## CODE AVAILABILITY

The MB-pol water model used in this work is publicly available at:

<http://paesanigroup.ucsd.edu/software/mbx.html>. All analysis codes used in this article are available from the authors upon request.

## REFERENCES

1. Nilsson, A. & Pettersson, L. G. M. The structural origin of anomalous properties of liquid water. *Nat. Commun.* **6**, 8998 (2015).
2. Gallo, P. *et al.* Water: A Tale of Two Liquids. *Chem. Rev.* **116**, 7463–7500 (2016).
3. Fransson, T. *et al.* X-ray and Electron Spectroscopy of Water. *Chem. Rev.* **116**, 7551–7569 (2016).
4. Tokushima, T. *et al.* High resolution X-ray emission spectroscopy of liquid water: The observation of two structural motifs. *Chem. Phys. Lett.* **460**, 387–400 (2008).
5. Guo, J.-H. *et al.* X-Ray Emission Spectroscopy of Hydrogen Bonding and Electronic Structure of Liquid Water. *Phys. Rev. Lett.* **89**, 137402 (2002).
6. Kashtanov, S. *et al.* Local structures of liquid water studied by x-ray emission spectroscopy. *Phys. Rev. B* **69**, 024201 (2004).
7. Zhovtobriukh, I., Besley, N. A., Fransson, T., Nilsson, A. & Pettersson, L. G. M. Relationship between x-ray emission and absorption spectroscopy and the local H-bond environment in water. *J. Chem. Phys.* **148**, 144507 (2018).
8. Tokushima, T. *et al.* High resolution X-ray emission spectroscopy of water and its assignment based on two structural motifs. *J. Electron Spectros. Relat. Phenomena* **177**, 192–205 (2010).

9. Sellberg, J. A. *et al.* X-ray emission spectroscopy of bulk liquid water in “no-man’s land”. *J. Chem. Phys.* **142**, 044505 (2015).
10. Nilsson, A. & Pettersson, L. G. M. Perspective on the structure of liquid water. *Chem. Phys.* **389**, 1–34 (2011).
11. Nilsson, A., Huang, C. & Pettersson, L. G. M. Fluctuations in ambient water. *J. Mol. Liq.* **176**, 2–16 (2012).
12. Fuchs, O. *et al.* Isotope and Temperature Effects in Liquid Water Probed by X-Ray Absorption and Resonant X-Ray Emission Spectroscopy. *Phys. Rev. Lett.* **100**, 027801 (2008).
13. Fuchs, O. *et al.* Fuchs et al. Reply: *Phys. Rev. Lett.* **100**, 249802 (2008).
14. Odelius, M. Molecular dynamics simulations of fine structure in oxygen K-edge x-ray emission spectra of liquid water and ice. *Phys. Rev. B* **79**, 144204 (2009).
15. Besley, N. A. Equation of motion coupled cluster theory calculations of the X-ray emission spectroscopy of water. *Chem. Phys. Lett.* **542**, 42–46 (2012).
16. Chandler, D. & Wolynes, P. G. Exploiting the isomorphism between quantum theory and classical statistical mechanics of polyatomic fluids. *J. Chem. Phys.* **74**, 4078–4095 (1981).
17. Parrinello, M. & Rahman, A. Study of an F center in molten KCl. *J. Chem. Phys.* **80**, 860–867 (1984).
18. De Raedt, B., Sprik, M. & Klein, M. L. Computer simulation of muonium in water. *J. Chem. Phys.* **80**, 5719–5724 (1984).
19. Berne, B. J. & Thirumalai, D. On the Simulation of Quantum Systems: Path Integral Methods. *Annu. Rev. Phys. Chem.* **37**, 401–424 (1986).
20. Babin, V., Leforestier, C. & Paesani, F. Development of a “First Principles” Water

- Potential with Flexible Monomers: Dimer Potential Energy Surface, VRT Spectrum, and Second Virial Coefficient. *J. Chem. Theory Comput.* **9**, 5395–5403 (2013).
21. Medders, G. R., Babin, V. & Paesani, F. Development of a “First-Principles” Water Potential with Flexible Monomers. III. Liquid Phase Properties. *J. Chem. Theory Comput.* **10**, 2906–2910 (2014).
  22. Babin, V., Medders, G. R. & Paesani, F. Development of a “First Principles” Water Potential with Flexible Monomers. II: Trimer Potential Energy Surface, Third Virial Coefficient, and Small Clusters. *J. Chem. Theory Comput.* **10**, 1599–1607 (2014).
  23. Burke, K., Werschnik, J. & Gross, E. K. U. Time-dependent density functional theory: Past, present, and future. *J. Chem. Phys.* **123**, 062206 (2005).
  24. Runge, E. & Gross, E. K. U. Density-Functional Theory for Time-Dependent Systems. *Phys. Rev. Lett.* **52**, 997–1000 (1984).
  25. Ullrich, C. A. & Yang, Z. A Brief Compendium of Time-Dependent Density Functional Theory. *Brazilian J. Phys.* **44**, 154–188 (2014).
  26. Feynman, R. P. *Statistical Mechanics: A Set Of Lectures*. (Avalon Publishing, 1998).
  27. Paesani, F. & Voth, G. A. The Properties of Water: Insights from Quantum Simulations. *J. Phys. Chem. B* **113**, 5702–5719 (2009).
  28. Ceriotti, M. *et al.* Nuclear Quantum Effects in Water and Aqueous Systems: Experiment, Theory, and Current Challenges. *Chem. Rev.* **116**, 7529–7550 (2016).
  29. Paesani, F. Getting the Right Answers for the Right Reasons: Toward Predictive Molecular Simulations of Water with Many-Body Potential Energy Functions. *Acc. Chem. Res.* **49**, 1844–1851 (2016).
  30. Reddy, S. K. *et al.* On the accuracy of the MB-pol many-body potential for water:

- Interaction energies, vibrational frequencies, and classical thermodynamic and dynamical properties from clusters to liquid water and ice. *J. Chem. Phys.* **145**, 194504 (2016).
31. Brown, S. E. *et al.* Monitoring Water Clusters “Melt” Through Vibrational Spectroscopy. *J. Am. Chem. Soc.* **139**, 7082–7088 (2017).
  32. Moberg, D. R. *et al.* The end of ice I. *Proc. Natl. Acad. Sci.* **116**, 24413–24419 (2019).
  33. Hunter, K. M., Shakib, F. A. & Paesani, F. Disentangling Coupling Effects in the Infrared Spectra of Liquid Water. *J. Phys. Chem. B* **122**, 10754–10761 (2018).
  34. Medders, G. R. & Paesani, F. Infrared and Raman Spectroscopy of Liquid Water through “First-Principles” Many-Body Molecular Dynamics. *J. Chem. Theory Comput.* **11**, 1145–1154 (2015).
  35. Medders, G. R. & Paesani, F. Dissecting the Molecular Structure of the Air/Water Interface from Quantum Simulations of the Sum-Frequency Generation Spectrum. *J. Am. Chem. Soc.* **138**, 3912–3919 (2016).
  36. Straight, S. C. & Paesani, F. Exploring Electrostatic Effects on the Hydrogen Bond Network of Liquid Water through Many-Body Molecular Dynamics. *J. Phys. Chem. B* **120**, 8539–8546 (2016).
  37. Pham, C. H., Reddy, S. K., Chen, K., Knight, C. & Paesani, F. Many-Body Interactions in Ice. *J. Chem. Theory Comput.* **13**, 1778–1784 (2017).
  38. Moberg, D. R., Straight, S. C., Knight, C. & Paesani, F. Molecular Origin of the Vibrational Structure of Ice I<sub>h</sub>. *J. Phys. Chem. Lett.* **8**, 2579–2583 (2017).
  39. Reddy, S. K., Moberg, D. R., Straight, S. C. & Paesani, F. Temperature-dependent vibrational spectra and structure of liquid water from classical and quantum simulations with the MB-pol potential energy function. *J. Chem. Phys.* **147**, 244504 (2017).

40. Moberg, D. R., Straight, S. C. & Paesani, F. Temperature Dependence of the Air/Water Interface Revealed by Polarization Sensitive Sum-Frequency Generation Spectroscopy. *J. Phys. Chem. B* **122**, 4356–4365 (2018).
41. Moberg, D. R., Sharp, P. J. & Paesani, F. Molecular-Level Interpretation of Vibrational Spectra of Ordered Ice Phases. *J. Phys. Chem. B* **122**, 10572–10581 (2018).
42. Gaiduk, A. P., Pham, T. A., Govoni, M., Paesani, F. & Galli, G. Electron affinity of liquid water. *Nat. Commun.* **9**, 247 (2018).
43. Sun, Z. *et al.* Electron-Hole Theory of the Effect of Quantum Nuclei on the X-Ray Absorption Spectra of Liquid Water. *Phys. Rev. Lett.* **121**, 137401 (2018).
44. Gilberg, E., Hanus, M. J. & Foltz, B. Investigation of the electronic structure of ice by high resolution X-ray spectroscopy. *J. Chem. Phys.* **76**, 5093–5097 (1982).
45. Michelitsch, G. S. & Reuter, K. Efficient simulation of near-edge x-ray absorption fine structure (NEXAFS) in density-functional theory: Comparison of core-level constraining approaches. *J. Chem. Phys.* **150**, 074104 (2019).
46. Kumar, R., Schmidt, J. R. & Skinner, J. L. Hydrogen bonding definitions and dynamics in liquid water. *J. Chem. Phys.* **126**, 204107 (2007).
47. Wernet, P. *et al.* The Structure of the First Coordination Shell in Liquid Water. *Science* (80-. ). **304**, 995–999 (2004).
48. Becke, A. D. A new mixing of Hartree–Fock and local density-functional theories. *J. Chem. Phys.* **98**, 1372–1377 (1993).
49. Woon, D. E. & Dunning, T. H. Gaussian basis sets for use in correlated molecular calculations. V. Core-valence basis sets for boron through neon. *J. Chem. Phys.* **103**, 4572–4585 (1995).

50. Dunning, T. H. Gaussian basis sets for use in correlated molecular calculations. I. The atoms boron through neon and hydrogen. *J. Chem. Phys.* **90**, 1007–1023 (1989).
51. Paesani, F., Zhang, W., Case, D. A., Cheatham, T. E. & Voth, G. A. An accurate and simple quantum model for liquid water. *J. Chem. Phys.* **125**, 184507 (2006).
52. Lestrangle, P. J., Nguyen, P. D. & Li, X. Calibration of Energy-Specific TDDFT for Modeling K-edge XAS Spectra of Light Elements. *J. Chem. Theory Comput.* **11**, 2994–2999 (2015).
53. Stetina, T. F., Clark, A. E. & Li, X. X-ray absorption signatures of hydrogen-bond structure in water-alcohol solutions. *Int. J. Quantum Chem.* **119**, e25802 (2019).
54. Liang, W., Fischer, S. A., Frisch, M. J. & Li, X. Energy-Specific Linear Response TDHF/TDDFT for Calculating High-Energy Excited States. *J. Chem. Theory Comput.* **7**, 3540–3547 (2011).
55. Hait, D. *et al.* Accurate prediction of core-level spectra of radicals at density functional theory cost via square gradient minimization and recoupling of mixed configurations. *J. Chem. Phys.* **153**, 134108 (2020).
56. Frisch, M. J. *et al.* Gaussian 16 Revision C.01. (2016).
57. Jones, R. O. & Gunnarsson, O. The density functional formalism, its applications and prospects. *Rev. Mod. Phys.* **61**, 689–746 (1989).
58. Hellman, A., Razaznejad, B. & Lundqvist, B. I. Potential-energy surfaces for excited states in extended systems. *J. Chem. Phys.* **120**, 4593–4602 (2004).

## **ACKNOWLEDGMENTS**

We thank Colin Egan and Saswata Dasgupta for a critical read of the manuscript, and Aurora Clark for stimulating discussions. This research was supported by the U.S. Department of Energy, Office of Science, Office of Basic Energy Science, through grant no. DE-SC0019490 (F.P.), and IDREAM (Interfacial Dynamics in Radioactive Environments and Materials), an Energy Frontier Research Center funded by the U.S. Department of Energy, Office of Science, Basic Energy Sciences. This research used resources of the National Energy Research Scientific Computing Center (NERSC), which is supported by the Office of Science of the U.S. Department of Energy under Contract DE-AC02-05CH11231, the Extreme Science and Engineering Discovery Environment (XSEDE), which is supported by the National Science Foundation grant number ACI-1548562, and the Triton Shared Computing Cluster (TSCC) at the San Diego Supercomputer Center (SDSC).

## **AUTHOR CONTRIBUTIONS**

V.W.D.C. and A.W. contributed equally to this work. A.W. and X.L. developed the theoretical TD-DFT approach, and V.W.D.C. and F.P. developed the QM/MM interface with the PIMD simulations carried out with MB-pol. V.W.D.C. performed the theoretical calculations, data analysis, and prepared the figures. F.P. and V.W.D.C. wrote the first version of the manuscript, and all authors contributed to the subsequent revisions. X.L. and F.P. designed and supervised the research.

## **COMPETING INTERESTS**

The authors declare no competing financial interest.

## ADDITIONAL INFORMATION

**Supporting information.** Details about the QM/MM TD-DFT and Delta SCF calculations, analyses of the theoretical  $1b_1$ -to- $1a_1$  lineshapes of liquid water and ice  $I_h$  as a function of the number of TD-DFT calculations. Description of the energy scale and convolution of the theoretical  $1b_1$ -to- $1a_1$  lineshape, definition of the Local Structure Index (LSI). Details about all H-bonding topologies and associated fractions extracted from the MB-pol PIMD simulations of liquid water and ice  $I_h$ .